Article:
Wilson, B.T., Robson, J.D., Shanthraj, P. et al. (2022) Simulating intergranular hydrogen enhanced decohesion in aluminium using density functional theory. Modelling and Simulation in Materials Science and Engineering, 30 (3). 035009. ISSN: 0965-0393

https://doi.org/10.1088/1361-651x/ac4a23

Simulating intergranular hydrogen enhanced decohesion in aluminium using density functional theory

OPEN ACCESS
IOP Publishing
Modelling and Simulation in Materials Science and Engineering
Modelling Simul. Mater. Sci. Eng. **30** (2022) 035009 (17pp) https://doi.org/10.1088/1361-651X/ac4a23

Simulating intergranular hydrogen enhanced decohesion in aluminium using density functional theory

Benjamin T Wilson*, Joseph D Robson, Pratheek Shanthraj and Christopher P Race

University of Manchester, Department of Materials, United Kingdom

E-mail: benjamin.wilson@manchester.ac.uk

Received 6 September 2021, revised 16 December 2021
Accepted for publication 11 January 2022
Published 17 February 2022

Abstract

Materials modelling at the atomistic scale provides a useful way of investigating the widely debated fundamental mechanisms of hydrogen embrittlement in materials like aluminium alloys. Density functional theory based tensile tests of grain boundaries (GBs) can be used to understand the hydrogen enhanced decohesion mechanism (HEDE). The cohesive zone model was employed to understand intergranular fracture from energies obtained in electronic structure calculations at small separation increments during *ab initio* tensile tests of an aluminium $\Sigma 11$ GB supercell with variable coverages of H. The standard rigid grain shift (RGS) test and a quasistatic sequential test, which aims to be faster and more realistic than the RGS method, were implemented. Both methods demonstrated the effects of H on the cohesive strength of the interface. The sequential method showed discrete structural changes during decohesion, along with significant deformation in general compared to the standard rigid approach. H was found to considerably weaken the GB, where increasing H content led to enhanced embrittlement such that, for the highest coverages of H, GB strength was reduced to approximately 20% of the strength of a pure Al GB—it is proposed that these results simulate HEDE. The possibility of finding H coverages required to induce this effect in real alloy systems is discussed in context by using calculations of the heat of segregation of H.

Keywords: hydrogen, embrittlement, dft, atomistic, decohesion, aluminium

(Some figures may appear in colour only in the online journal)

*Author to whom any correspondence should be addressed.

1. Introduction

Following decades of research into hydrogen embrittlement (HE) in metallurgy, its mechanistic origin remains a widely debated topic [1]. Understanding how and why HE occurs is an important issue for the design of structural metallic materials, particularly on modern aircraft, where there is robust evidence of HE in the form of H environment assisted cracking (HEAC) at grain boundaries (GBs) in high-strength Al alloys [2]; experimental work on this issue is challenging due to the low equilibrium solubility of H in Al [3]. Most pertinent to Al and its alloys are four major varieties of HE mechanisms, all of which fall under the generalism of H weakening interatomic bonds of the Al crystal [4]. Combinations of competing HE mechanisms, and synergistic hybrid mechanisms [5], are most likely involved, subject to environmental and metallurgical conditions [6]. Component mechanisms are widely debated, with H enhanced decohesion (hydrogen enhanced decohesion mechanism (HEDE)), H enhanced localised plasticity, adsorption induced dislocation emission (AIDE), and hydride formation being routinely propounded as potential candidates [4, 7]. Evidence of featureless fracture surfaces point to an HEDE [8], which posits that H along GBs (or cleavage planes in the case of transgranular cracking) reduces the cohesive binding energy of an interface before fracture [9].

Modern computational capabilities have spawned efforts to model HE using an *ab initio* approach, where embrittlement mechanisms are explored by circumventing the challenges associated with experimental measurements of H in Al alloys [10]. A thermodynamic framework has been developed by Rice and Wang to quantify this embrittlement using a cohesive zone fracture model (CZFM) [11], which has been explored for Al at the atomistic scale using density functional theory (DFT) based *ab initio* tensile tests (AbTTs) [12–15]. Typically these tests make use of the rigid grain shift (RGS) method following the work on universal binding energy relationships introduced by Rose *et al* [16], however Van der Ven *et al* adopted an elongation approach whereby their computational cell in an atomistic model is uniaxially homogeneously strained [13]; this method notably recovered the behaviour of Rose's universal binding for large elongations steps, but provides a phenomenologically different result for smaller elongation steps as the strain becomes less localised to one plane or interface. In the samer manner, Janisch *et al* [14] further investigated the differences between homogenous straining and RGS, where it was discovered that homogenous straining yields markedly different behaviour (decohesion is not localised at the interface) to the rigid approach that applies to the universal binding curve [16].

Ab initio methods enable incomparable control over system conditions relative to experimentation. The addition of segregant elements, such as alloying elements, and their interaction with GB strength and energetics has been used to investigate Al GB embrittlement [13, 17, 18], and more recently to H embrittlement where simulations show promising results in support of the HEDE hypothesis [12, 15]. *Ab initio* calculations from Zhang *et al* [17] revealed the nature of Al GB embrittlement by Zn segregation, showing how Al–Zn bonds were weaker than Al–Al. Later, Zhao *et al*, using RGS [18], established the embrittlement potency of Mg, and strengthening properties of Cu, to an Al GB via the same electronic mechanisms as [17]. Elsewhere, simulations have been performed for other metallic systems with a variety of embrittleing and strengthening agents. For example C has been shown to strengthen Mo GBs [19], S is shown to weaken Cu GBs [20], and the dual embrittling action by S and H in Ni GBs has been demonstrated [21]. Connecting atomistic results to macroscopic phenomena is an active area of research [10, 22, 23] involving larger scale finite element or phase-field simulations using the CZFM framework [24, 25]. Many larger scale models

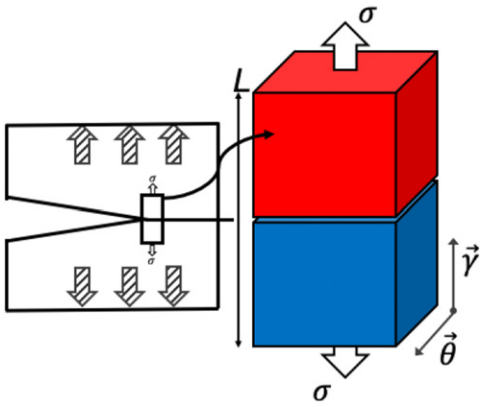

Figure 1. CZFM: A cohesive zone exists immediately ahead of the crack tip which is encompassed by a CE shown as two grains (red and blue) with the cohesive zone being the GB interface for an intergranular crack. A symmetric tilt grain boundary is described by a normal vector $\vec{\gamma}$ and a perpendicular rotation axis $\vec{\theta}$. A microscopic traction σ acts parallel to $\vec{\gamma}$, the corresponding strain results in extension in the length L of the CE.

adopt a consideration of H transport during fracture [5, 25]; moreover, successful multi-scale modelling has been applied to other metals, such as the impact of S embrittlement of Cu GBs [26].

In this work, we introduce a sequential grain shift (SGS) method for AbTTs as an improvement on the RGS method, which should reduce the computational time required to perform these tests and more accurately model the dynamical evolution of atoms during intergranular fracture. The RGS and SGS methodologies are here applied to a $\Sigma 11$ Al GB with variable H coverage to then evaluate the plausibility of the HEDE hypothesis. Advantages of each method, and their implications in helping to understand the HEDE mechanism, are latterly discussed.

2. Theory and methods

Brittle intergranular fracture theory developed by Rice & Wang [11] extends the Griffith theory to incorporate finer details of separation by using cohesive zones. A CZFM considers a small section of an interface, the cohesive zone, immediately ahead of a crack tip which will separate during crack growth (see figure 1). We take a cohesive zone and consider a small volume of material extending above and below the interface which we call a cohesive element (CE); crack propagation is seen as successive failures along a series of CEs. CZFMs assume linearly elastic behaviour in the regions surrounding a CE, where macroscopic loads (i.e. a fracture stress) on the material will generate an atomistic traction $\sigma(\delta)$ applied perpendicular to the GB plane, with an atomistic granular separation δ. A CE fails when the bonding across its interface is completely broken such that the two fracture surfaces are displaced past their interaction range δ_f. The work of separation W is the energy required to separate the grains from $\delta = 0$ to δ_f. AbTTs complement the CZFM by including atomistic behaviour in CE modelling.

CEs, as shown in figure 1, contain two grains with a fixed number of Al atoms, each having a face centred cubic crystal structure. We define a GB plane with unit normal vector $\vec{\gamma}$, and a rotation axis $\vec{\theta}$ about which the grains are misoriented. GBs with orthogonal vectors ($\vec{\gamma} \cdot \vec{\theta} = 0$), like the one shown in figure 1, are pure tilt GBs. Atomistic modelling of GBs usually limits simulations to molecular configurations of special symmetric boundaries, which can

be described using the coincident site lattice model [27]. We selected a symmetric tilt $\Sigma 11$ GB with a normal vector $\vec{\gamma} = [\bar{1}13]$ crystal plane with a rotation axis $\vec{\theta} = [110]$ and misorientation angle of 129°.

Traction was modelled as a uniaxial tensile stress σ along $\vec{\gamma}$, and the corresponding separation is quantified by the change in length of the CE, $\delta = L - L_0$, where L_0 is the equilibrium length of the CE when $\sigma = 0$. δ is also called excess length, and similarly other excess parameters can be defined for variables which change according to the extent of the deformation δ. By assuming that the CE is embedded in a bulk material with uniform properties, the fundamental thermodynamic relation of excess (Helmholtz) free energy per unit area for a CE is given by the following differential [28],

$$\mathrm{d}F = -S\mathrm{d}T + \sigma\,\mathrm{d}\delta + \mu_{\mathrm{H}}\,\mathrm{d}\Gamma_{\mathrm{H}}. \tag{1}$$

The first term on the right-hand side of (1), $-S\mathrm{d}\,T$, represents the heat flow into the system. The second term, $\sigma\mathrm{d}\,\delta$, is an approximation of the mechanical work done to a CE. For simplicity we neglected self consistent structural coupling with the surrounding bulk, thus our approach did not capture any Poisson effect in a CE; regardless, expansion due to the Poisson effect is assumed to be negligible. The final term in (1) accounts for changes induced by the chemical potential, μ_{H}, and coverage, Γ_{H}, of a segregant impurity, H. In this study, we keep the impurity coverage and temperature fixed in all simulations, i.e. $\mathrm{d}\Gamma_{\mathrm{H}} = \mathrm{d}T = 0$, so that a change in free energy is strictly a result of mechanical work applied to the CE. Under these conditions, excess free energy, ΔF, can be derived as a function of δ from (1),

$$\Delta F(\delta) = \int_0^{\delta} \sigma(\delta')\mathrm{d}\delta'. \tag{2}$$

The strength of a CE is fundamentally derived from interatomic bonding. Generally, intergranular fracture is due to intergranular bonds being significantly weaker than interplanar bonds within grains. First-principles simulations can be used to model decohesion as the stretching and breaking of molecular bonds which exist across the crack path. This can be suitably accomplished by implementing a quantum mechanical treatment of electronic structure through Kohn–Sham DFT. Application of DFT requires consideration of a compromise between accurately representing true atomistic behaviour and computational feasibility; generally DFT calculations are made to predict the ground state energy of a static system of 10 s of atoms [29]. DFT avoids the requirement for an empirical Al–H potential, as used in molecular dynamics, and instead makes direct quantum mechanical predictions of the Al–H interaction. We use calculations of a system's excess energy in DFT as an approximation to the thermodynamic excess free energy of (2) at $T = 0$ K. AbTT results are used to obtain W, δ_f, critical traction for fracture σ_{c}, and critical displacement δ_{c} at σ_{c}, properties which are collectively referred to as a traction-separation law for a CZ [13, 30]; these laws can be implemented as parameters in larger scale continuum CZFMs, but this is not in the scope of this paper [24].

We used the Vienna *ab initio* simulation package [31–34] with the projector augmented wave method [35, 36] for DFT *ab initio* energy calculations. A Monkhorst-Pack k-point mesh [37] of $5 \times 13 \times 2$ k-points was used, giving a linear density of 1.3, 0.8, and 1.4 nm along the (reciprocal) $\vec{\gamma} \times \vec{\theta}$, $\vec{\theta}$, and $\vec{\gamma}$ axes respectively. A plane wave cut off energy of 400 eV, using the k point mesh above, was found to be sufficient for an accuracy of 1 meV/atom for an Al grain boundary cell comprised of 70 atoms and two GBs. The PBE GGA exchange-correlation functional [38, 39] is used throughout, along with Methfessel–Paxton smearing of 0.2 eV [40]. Electronic structure was optimised using the Block–Davidson method [41] with a convergence criterion of 0.1 meV. We used a conjugate gradient algorithm for geometry optimisation

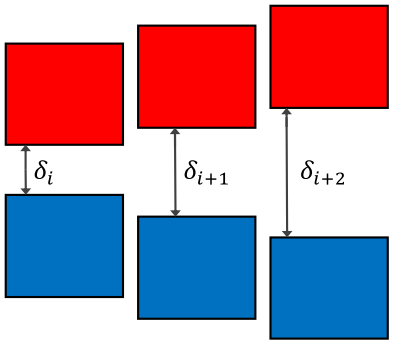

Figure 2. RGS of a CE (figure 1) for three different separation increments along $\vec{\gamma}$. The RGS AbTT takes a set of n RGS and calculates the internal energy of the system at each shift.

[42, 43] to relax ions into their instantaneous ground state, with a displacement increment of 1.5×10^{-3} nm and a convergence criterion of 1 meV/atom. A sequential application of an increment of displacement, optionally followed by internal relaxation of the ionic coordinates, results in a simulation of an external stress generating an atomistic scale traction, σ, which strains a GB until fracture, hence the term AbTT.

The RGS methodology is a commonly used approach to apply σ to a CE in AbTTs (see figure 2) [14]. A pure RGS approach constructs a set of n CE cells with the equilibrium lattice geometry fixed in each grain, in each CE cell the top grain is shifted away from the bottom grain by a separation increment δ_i, where $\delta_0 = 0$ and $\delta_n > \delta_f$. An energy calculation is made at each separation increment, with the ionic positions of each atom unchanged within their respective grains. The RGS excess free energies $\Delta F_{\mathrm{RGS}}(\delta_i)$ are calculated as the difference between the energy at each RGS and the equilibrium ($\delta = 0$) CE. RGSs have been further developed to include ionic relaxation at each shift which will be denoted as RGS + X, the excess free energies calculated using this second method are labelled $\Delta F_{\mathrm{RGS+X}}(\delta_i)$.

We present a third approach, SGS, which deviates from the standard RGS method by including a quasistatic evolution of the ionic structure during decohesion. We inserted a small layer of vacuum along the GB with thickness 0.025 nm, this is a grain shift. We then allowed the ions to relax using the CG algorithm [42, 43]. Taking the relaxed geometry, we inserted another vacuum layer in the centre of the previous layer (applying another grain shift) and optimised ionic positions again. This process was repeated until the added volume to the CE was 0.625 nm along $\vec{\gamma}$, sufficient to exceed the range of any intergranular interactions. To speed up calculations, ions which were more than two atomic layers away from the GB were frozen during ionic position optimisations.

We fitted the energies of the RGS and RGS + X tests to a fitting function,

$$\Delta F_{\mathrm{fit}}(\delta) = W\left[1 - \left(\bar{\delta}_m + 1\right) e^{-\bar{\delta}_m}\right], \tag{3}$$

where $\bar{\delta}_m$ is an mth order polynomial function of δ with fitting parameters λ_i,

$$\bar{\delta}_m = \sum_{i=1}^{m} \left(\delta/\lambda_i\right)^{2i-1}. \tag{4}$$

The results from the pure RGS approach were fitted with an $m = 1$ form, which analytically recovers the universal binding energy relationship proposed by Rose *et al* [16]. We used an $m = 2$ form to fit the energies of the RGS + X method, which is equivalent to the modified relationship proposed by Srirangarajan *et al* [44]. Traction can then be derived from the fitted energies by using an analytical derivative of (3):

$$\sigma_{\text{fit}}(\delta) = \frac{\mathrm{d}\Delta F_{\text{fit}}}{\mathrm{d}} = \left(\frac{\mathrm{d}\bar{\delta}_m}{\mathrm{d}\delta}\right) W\bar{\delta}_m e^{-\bar{\delta}_m}. \tag{5}$$

The SGS tests are, as shown in the results section, unsuitable to this type of curve fitting procedure—therefore traction under this regime is obtained from a numerical derivative of ΔF_{SGS} using finite central differences, δ_c is found at the peak of the numerical derivative, and δ_f is estimated using (6) [19]. These SGS parameters can be assembled into a bilinear traction-separation law [45]

$$\delta_f = \frac{2W}{\sigma_{\text{c}}}. \tag{6}$$

Segregation of impurities to a GB depends on the Gibb's free energy of segregation ΔG_{seg} which is used in models of interface concentrations, e.g. Langmuir–Mclean theory [46]. ΔG_{seg} is the sum of two terms: the heat of segregation, ΔH_{seg}, and the segregation entropy, $T\Delta S_{\text{seg}}$. In these models, the atomic fraction of impurity is completely determined for a given temperature and composition. Our AbTT results allow us to obtain the standard heat of segregation component of ΔG_{seg}. We include N_{H} (=0 to 10) H atoms in multiple configurations in interstitial voids on the GB plane, leading to a total of 11 closed GB structures for AbTTs. Ten large voids were identified on the GB plane for distributing N_{H} atoms. The occupation of these voids for each N_{H} was determined by, firstly, finding the most energetically favourable site for $N_{\text{H}} = 1$ after ten energy calculations with optimised ionic geometries for each void. Then, secondly, finding the most energetically favourable site for each additional H atom using the same method, excluding the option of H occupying a void already containing H; consequently we do not consider H_2 molecules. Given that there are 12 Al atoms on the GB in H-free structures, the GB H coverage can be defined in (7),

$$\Gamma_{\text{H}} = \frac{N_{\text{H}}}{12 + N_{\text{H}}}. \tag{7}$$

The standard heat of segregation, ΔH_{seg}, for a single H atom was determined as the difference between the solution enthalpy for an H atom at the GB of the CE, $\Delta H^{\text{GB}}_{\text{sol}}$, and in a tetrahedral interstice in the bulk region of the CE, $\Delta H^{\text{B}}_{\text{sol}}$. For multiple H segregation, we adopt a simplified approach which requires us to calculate the free energy of a CE containing one H atom in the bulk and none at the boundary, and then subtract the free energy of a CE with no H at all to obtain $\Delta H^{\text{B}}_{\text{sol}}$. We obtain $\Delta H^{\text{GB}}_{\text{sol}}$ as the difference in free energies of a CE containing Γ_{H} and a CE with no H. The advantage of this approach is that we can calculate an average ΔH_{seg} per H atom as a function of δ by using separated CEs in the calculation of $\Delta H^{\text{GB}}_{\text{sol}}$ in (8),

$$\Delta H_{\text{seg}}(\delta, \Gamma_{\text{H}}) = \Delta H^{\text{GB}}_{\text{sol}}(\delta, \Gamma_{\text{H}})/N_{\text{H}} - \Delta H^{\text{B}}_{\text{sol}}. \tag{8}$$

3. Results

The geometry of a 70 Al atom H-free CE was obtained by first generating two grains with lattice constants of 0.404 nm. Our $\Sigma 11$ GB was found to have a GB energy of 1.19 eV nm^{-2}.

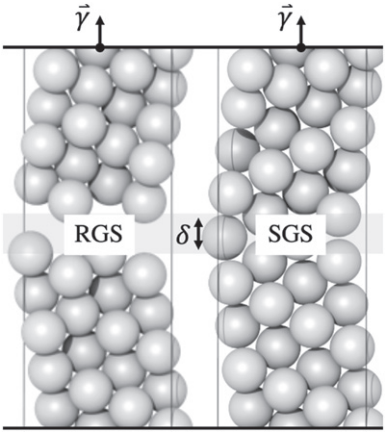

Figure 3. Strained CE's separated by a granular displacement δ for RGS and SGS AbTTs. Periodic boundary conditions mean there are two GBs in the CE, but we keep the untested boundary interatomically rigid. GB healing in the SGS test (right) means atoms fill the entire CE, whereas no healing can occur in a purely RGS test (left).

We applied three tensile test approaches to our CE at 11 different impurity coverages $\Gamma_H = 0$ to 45 at%: RGS, RGS + X, and SGS. Following the tests it was observed that the length of the CE along $\vec{\gamma}$ was optimised in the $\Gamma_H = 0$ state by an expansion of 2.13 $\times 10^{-2}$ nm, which is accounted for in all three test methods. Figure 3 shows the stark difference in lattice geometry at $\delta = 0.45$ nm for the RGS and SGS tests with $\Gamma_H = 0$. Under the dynamic approach, there is considerable lattice strain in each grain which we refer to as GB healing.

Figure 4 shows the excess energies calculated using the RGS(+X) and SGS methods. For the RGS(+X) methods, it appears that for low coverages of H the GB becomes stronger than the clean $\Gamma_H = 0$ GB. However there is significant embrittlement at high coverages above $\Gamma_H = 29$ at%. These results may be explained by the instability of H on free Al surfaces at the end of the simulation. In the RGS + X approach the effect of GB strengthening for low Γ_H is reduced by allowing H and the surfaces to relax into a more favourable geometry. But still, there is a very small strengthening effect from low Γ_H up to 14 at%. On the other hand, the embrittlement potency of H at higher coverages is calculated to be stronger in RGS + X than in the RGS tests alone, again a result of more stable fracture surfaces. For the SGS test we observe a steady decrease in GB strength with increasing Γ_H. Under the SGS regime at $\delta \sim 0.4$ nm the structure undergoes a sudden discontinuous transition from a highly strained metastable healed structure to a lower energy two-surface configuration, which we refer to as snapping. During preliminary testing, the extent of healing was found to be sensitive to the size of the separation increments: fine δ simulations undergo significant healing while coarse δ simulations will snap earlier in the test.

To understand the fitting accuracy of each approach we plot the mean absolute error,

$$\text{m.a.e} = \frac{1}{N_\delta} \sum_i |\Delta F_{\text{fit}}(\delta_i) - \Delta F_{\text{AbTT}}(\delta_i)|, \tag{9}$$

for each style of test as a function of Γ_H (figure 5), where $\Delta F_{\text{AbTT}}(\delta_i)$ are the DFT calculated results from our AbTTs. The RGS + X fit performed best, maintaining an error of less

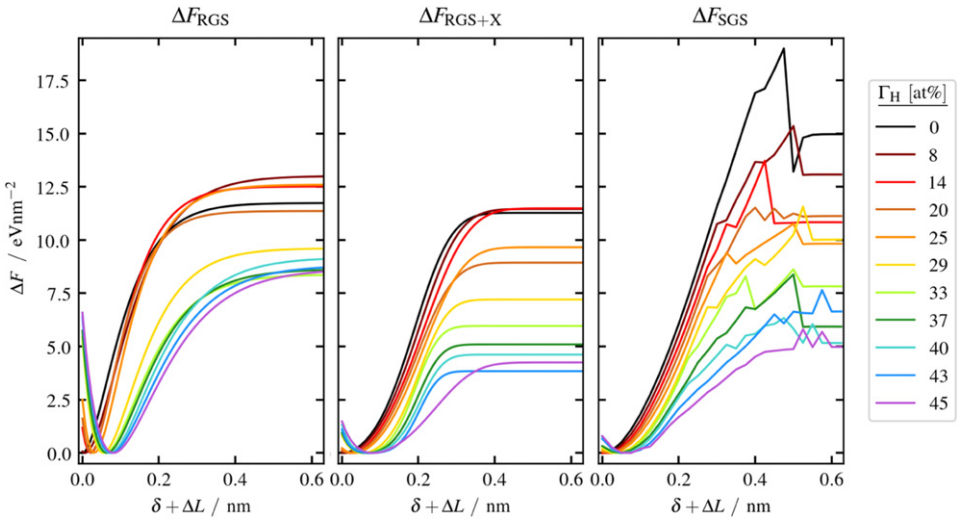

Figure 4. Excess free energies during separation of a grain boundary containing different coverages, Γ_H, of H. Left (and centre) are the results of the RGS(+X) tests using the fitting equation (4), and right are the results of the SGS tests, see figure 5 to assess the accuracy of the fitting equations. Separations, δ, include the expansion of the cell, ΔL, caused by the inclusion of H on a clean boundary for an easier visual comparison of the system behaviour for small δ.

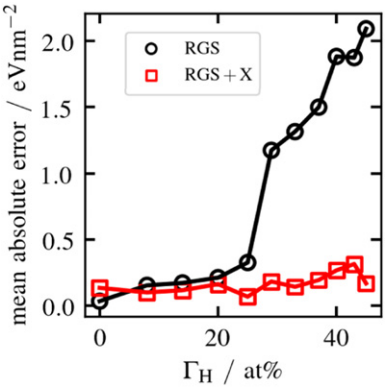

Figure 5. Mean absolute error of the fitting fucntions for the RGS and RGS + X tests at each coverage, Γ_H, of H, calculated according to equation (8).

than 0.3 eV nm^{-2} across all impurity coverages. The pure RGS fit does well for low impurity coverage, but becomes intolerable for high Γ_H.

Figure 6(a) shows the work of separation for each style of test. The pure RGS tests show a weak trend of decreasing W with increasing Γ_H but, as mentioned above, the RGS results are not considered accurate for high Γ_H. Despite a significant difference between RGS + X and SGS at $\Gamma_H = 0$, these two approaches follow a similar strong downward trend in W with increasing Γ_H. Using data from the SGS tests, W was reduced by 13% for the lowest H coverage $\Gamma_H = 8\%$—this effect becomes more pronounced for higher coverages where it was found that

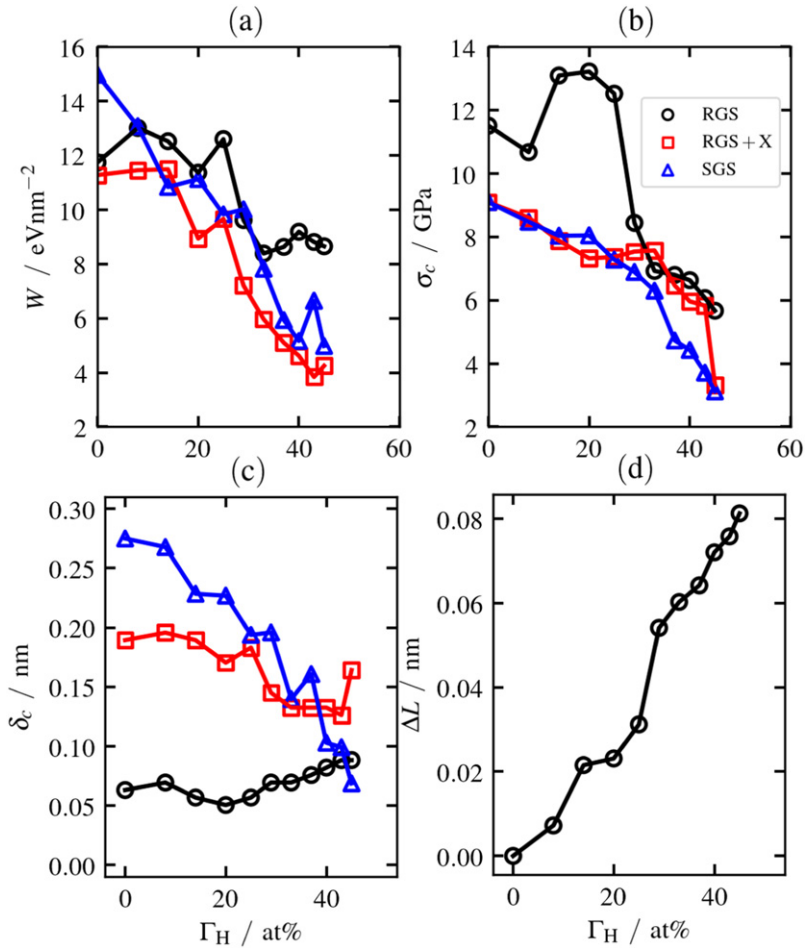

Figure 6. (a) Work of separation, W, plotted as a function of GB H coverage, Γ_H, for all three simulation methods. (b) Critical traction, σ_c, plotted as a function of GB H coverage, Γ_H, for all three simulation methods. (c) Critical displacement, δ_c, plotted as a function of GB H coverage, Γ_H, for all three simulation methods. (d) Change in length of a CE, ΔL, induced by the dissolution of H into a closed GB before traction is applied.

$\Gamma_H = 25\%$ reduced W by 35% and in the case of the highest coverage, $\Gamma_H = 45\%$, W was found to be 67% smaller than for the clean GB.

Traction was analytically derived using (5) for the RGS(+X) tests and numerically for the SGS test, and is shown in figure 7; all tests demonstrate GB weakening due to increasing levels of H. Due to the discontinuity in the SGS simulation, figure 7 plots traction up to the maximum point before snapping, since the derivative of a discontinuous function is undefined. Figure 8 shows the SGS derived bilinear traction-separation law [45] using δ_f values calculated from (6), we observe that an increasing Γ_H influences the traction separation law by reducing δ_c and increasing δ_f—this is a standard feature of embrittlement. Figure 6(b) plots the critical traction for each test method. Similar to W, σ_c has a strong downward trend with increasing Γ_H for both the RGS + X and SGS tests. Fractional reductions in σ_c are greater than for separation energies due to H; using the same three coverages mentioned above ($\Gamma_H = 8\%$, 25%, and 45%)

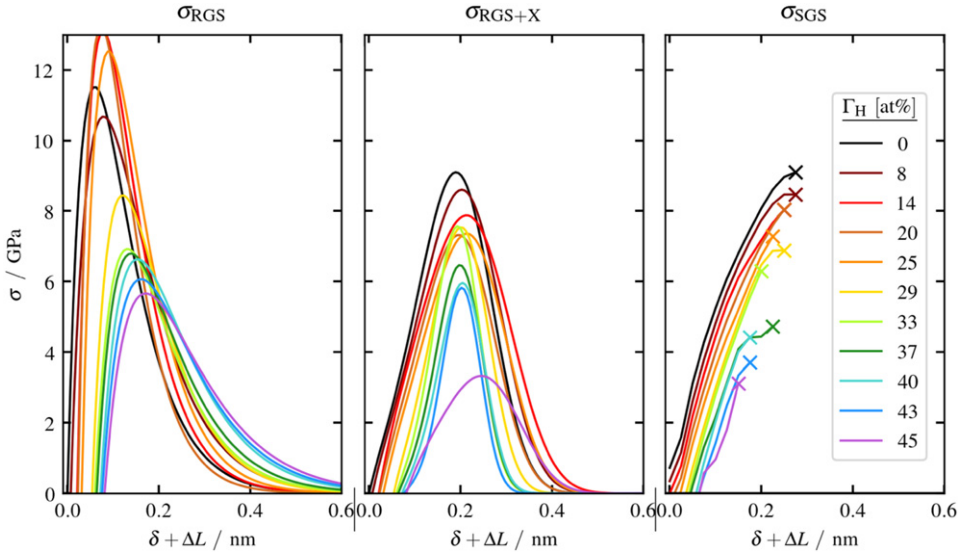

Figure 7. Traction separation curves for the RGS + X tests (left and centre), derived analytically from the fitting functions, and SGS (right), derived numerically up to the maximum point.

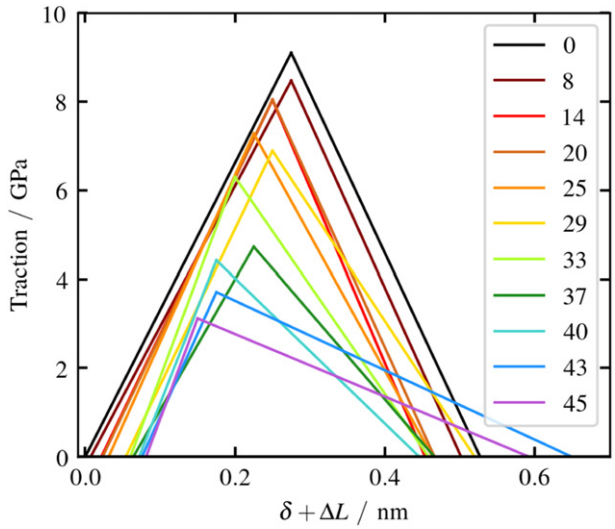

Figure 8. Bilinear traction-separation law derived from the SGS tests using (6), coloured according to Γ_H in at%.

the critical tractions obtained from the numerical results are reduced by 7%, 20%, and 66% respectively. The critical separation, figure 6(c), also follows this trend, but much more weakly. Even though the SGS results are sensitive to the separation increment size in a way that the RGS + X results are not, the critical tractions are very closely matched, implying that this sensitivity is to some degree immaterial to the critical traction.

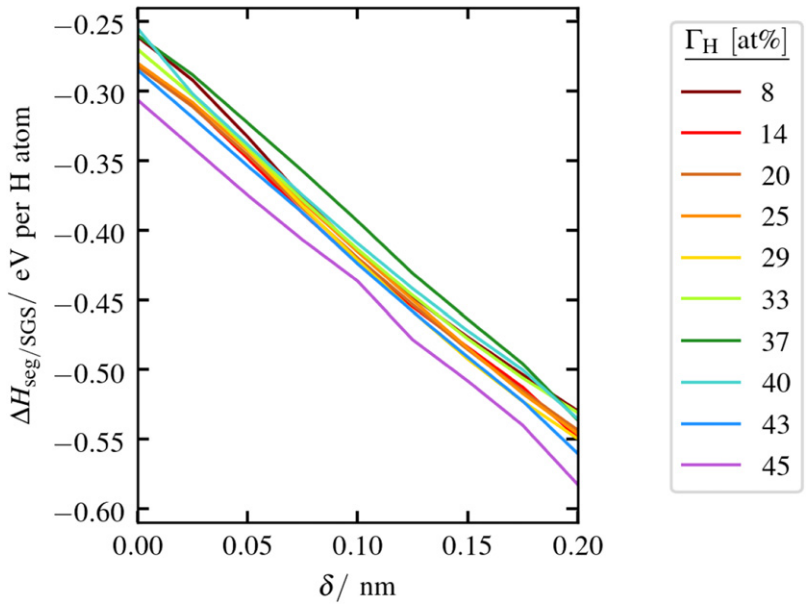

Figure 9. Average heat of segregation, ΔH_{seg}, for a single H atom to a GB, when given a prexisting coverage of GB H, Γ_H—these results, taken from the SGS simulations, show ΔH_{seg} plotted against GB separation, δ, for each Γ_H.

Figure 6(d) shows the changes in L_0, the equilibrium length of a CE, for different coverages of H. As expected we find a steady expansion of the GB with increasing Γ_H. For low δ, H's heat of segregation to the GB linearly decreases with increasing separation (figure 9). This is true for both RGS + X and SGS tests. Additionally, there is little difference between ΔH_{seg} values at different Γ_H; the largest difference is 36 meV, whereas the heat of segregation for a single H atom to a clean GB is calculated to be 261 meV, a much larger value than the differences between pre-existing H content. Recalling that ΔH_{seg} is the average enthalpy per H atom, this result suggests that the solution enthalpy for H at the GB does not vary according to GB coverages in this range.

Figure 10 shows ΔH_{seg} for the closed and fractured GBs. The flat trend at $\delta = 0$ confirms that ΔH_{seg} does not vary with Γ_H. ΔH_{seg} to free surfaces at low Γ_H is dependent on the *AbTT* method applied; the differences come from significant structural changes occurring in the SGS test to accommodate the impurity ions. For higher coverages of Γ_H, the two methods tend to converge with the SGS method producing more stable final structures.

The raw DFT data and geometry files are available online as supplementary material, along with a python notebook for quick analysis: www.zenodo.org/record/5763935.

4. Discussion

The GB energy of the (H free) $\Sigma 11$ GB (1.19 eV nm^{-2}, or 0.19 J m^{-2}) was found to be slightly higher than that calculated in a recent paper by Yamaguchi *et al* [15]. Using the PBE functional with a similarly scaled *k*-point mesh and a lower energy cut-off, they found a lower GB energy (1.06 eV nm^{-2}, or 0.17 J m^{-2}) which, given the similar method, might be attributed to differences in the details of the molecular configuration of the GB in [15]. Nevertheless, as shown

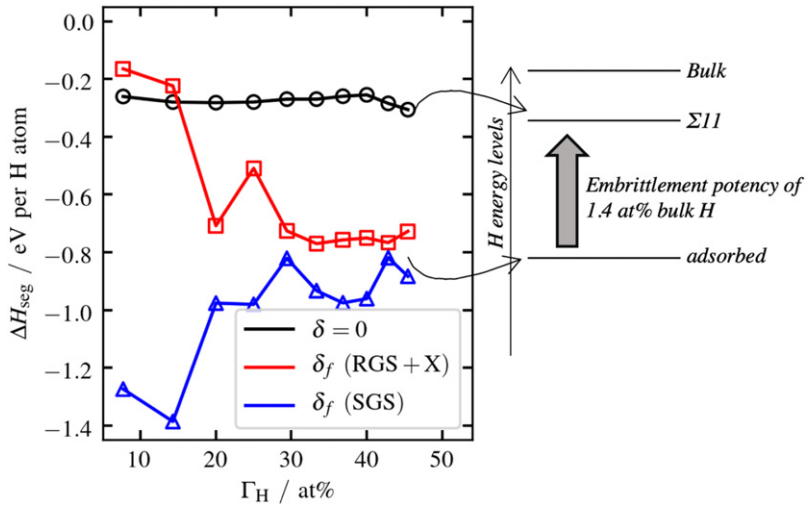

Figure 10. Average heat of segregation, ΔH_{seg}, to closed GBs (black) and fracture surfaces (red/blue). Right is an energy level diagram to show the embrittlement potency of a segregant, which is given by a positive energy difference between the closed GB state, Σ11, and the adsorbed state on a fracture surface—a diagram with a negative energy difference (as would occur for the lowest two Γ_H RGS + X simulations) would indicate GB strengthening from the segregant.

by [15], the difference is small relative to differences with other geometries (Σ3, Σ5, and Σ9), while another study calculated a larger GB energy (1.26 eV nm^{-2}, or 0.20 J m^{-2}) [47] by using the LDA functional. The initial expansion of 2.13 $\times 10^{-2}$ nm is also found to be slightly less than an LDA calculation by Janisch *et al* of 3.11 $\times 10^{-2}$ nm with a lower GB energy of 1.07 eV nm^{-2} (0.17 J m^{-2}) [14].

The results of figure 6(a) were equally obtained for Σ3, Σ5, and Σ9 GBs via an indirect method in [15] by Yamaguchi *et al* using calculations of only a closed ($\delta = 0$) and completely separated ($>\delta_f$) GB. Without performing AbTTs, they effectively derive W for RGS + X tests, and in some cases achieve higher Γ_H values than in this present study. From what we can now understand from figure 6(a), RGS + X and SGS tests give similar cohesive energies, therefore it is fair to argue that calculating only the final δ_f and initial states of the system is sufficient in order to quickly understand the broad embrittlement effects of a high coverage of H. It is, however, necessary to fully relax the geometry of the system, as demonstrated by figure 5 which shows that purely RGS type tensile tests modelled with Rose's UBER are inapplicable to highly defected GBs. It was found in [15] that W '*decreases almost linearly*' with Γ_H, and, in cases with roughly >20 atoms per nm^2 of GB, W can fall below 0 (the largest Γ_H that we consider includes 19 atoms per nm^2 of GB). These results imply spontaneous GB breaking if we were to increase the range of Γ_H we study, and it is concluded in [15] that this is because ΔL becomes so large for higher values of Γ_H that Al atoms are no longer metallically bonded across the interface.

In terms of the involvement of HE in HEAC phenomena in Al alloys (which are sensitive to environment humidity levels), the presence of such a high amount of GB H is not well evidenced, but it is predicted that freshly exposed Al surfaces will produce extremely high fugacity atomised H due to surface reactions with water vapour present [3]. In addition, Lynch notes that if slip planes are favourably aligned between grains at the GB, HE in the form of

AIDE is likely to occur at lower stresses [1]. It has been argued from strain-gradient plasticity studies that such high concentrations can exist locally as a result of deformation [48], this could occur in the plastic zone ahead of an intergranular crack tip for instance, but this is difficult to measure experimentally. It is further suggested in [15] that segregation energy (equivalent to the standard heat of segregation at $T = 0$ K) for separated GBs is much lower than in the closed state, this is also demonstrated in figure 10 for all but the lowest coverages of Γ_H in the RGS + X case. [15] equally corroborates that incremental additions of H do not impact heat of segregation, as indicated by a flat line for $\delta = 0$ in figure 10, although for high enough H coverages GB expansion passes a critical point where heat of segregation decreases, which we find to occur at around $\Gamma_H = 40$ at% for our $\Sigma 11$ GB.

The concept of dynamic embrittlement, applying to slow crack propagation scenarios, was initially explored in Al by Van der Ven and Ceder [13], but has more recently been applied by Ehlers *et al* [12]. The idea behind this process is that during separation, Γ_H is not fixed, and the thermodynamic potential to be minimised in the quasi-static regime is now the grand potential $\Omega = F - \mu_H \Gamma_H$, or, more appropriately, the grand force potential. Diffusion of H (from either the matrix or the environment of a crack tip) is hypothesised to be fast enough to respond to a decreasing heat of segregation shown in figure 9. This in turn would lower the traction required for further separation, as highlighted in figure 7. Ehlers *et al* stress the importance of finite temperature effects [12], especially when considering the relocation of H into more preferable sites during separation. At $T \sim 300$ K segregation of H does not readily occur in Al, but small deformations like the small displacements shown in figure 9 can dramatically alter the heat of segregation. The relationship between ΔH_{seg} and δ has been described as monotonic in [12]; which is roughly the result from our simulations too (figure 9). By any means, the effects of variable Γ_H and T will change the mechanisms of fracture in a meaningful way, but a simple deduction favours the idea that any dynamic embrittlement behaviour would exacerbate HEDE. On a larger scale, coupled decohesion-diffusion models can be applied to assess H induced fracture on physically relevant material geometries (such as a plate or rod) using phase-field formulations [25], kinetic models [26], and even employing discrete dislocation dynamics to consider non HEDE based HE [5], but discussing and evaluating the physical relevance of these models is beyond the scope of this paper which is focussed on molecular configurations in the decohering region only.

RGS and RGS + X tensile tests involve a predetermined failure mode, i.e. simulations have an artificially defined fracture path of bonds to break. For clean Al GBs the correct fracture path is easily identified by symmetry as the bonds across the GB plane, but with impurities the failure mode is less predictable. Any lattice defects in the CSL GB must be artificially assigned to the correct grain when using an RGS method. If there is a high concentration of impurities in the CE at the GB then it would take considerable work to correctly predict which impurities will be assigned to which grain when the grains are shifted. On the contrary, SGS simulations allow atoms to be exchanged across the GB according to DFT calculated interatomic forces. An alternative approach is to homogeneously strain the CE along $\vec{\gamma}$ in what are called drag simulations [14]. Homogenous straining inevitably introduce less accurate input geometries for ionic optimisation, especially for small δ, because the strain isn't localised to the decohering region, which means a greater computational cost over grain shift counterparts with frozen cores. On top of this, SGS tests are faster than RGS methods, also due to better input geometries for optimisation—in RGS + X tests nearly identical atomic relaxations from the undeformed geometry are repeated at each step, and it is this repetition which is evaded by SGS.

The physical relevance of homogenous straining over our SGS method is debatable. Using nudged elastic band calculations to investigate the effects of finite temperatures on the stability

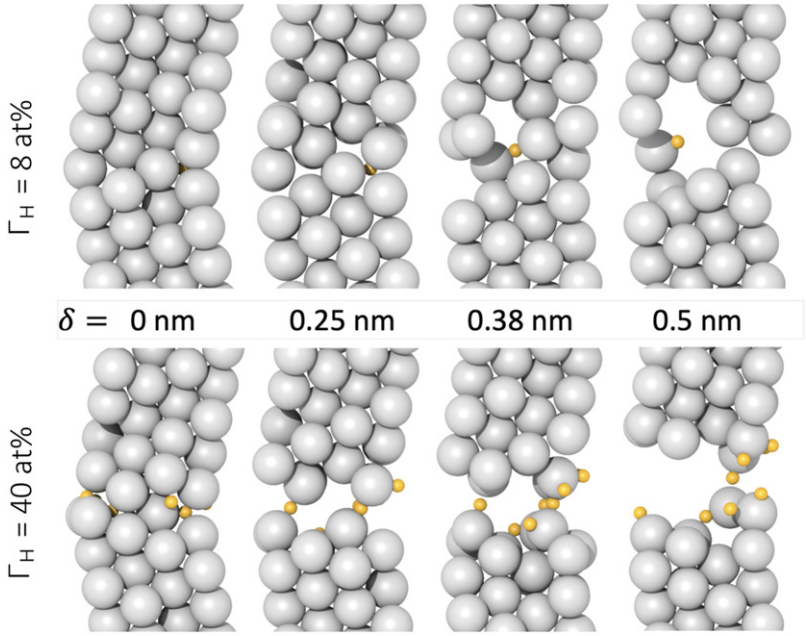

Figure 11. Snapshots of the SGS AbTT simulations for four of the X separation increments, δ_i, at two different GB H coverages, Γ_H. The extent of GB healing is more pronounced at lower coverages of Γ_H, therefore suppression of GB healing for higher coverages is proposed to be a component of the HEDE mechanism.

of the structures obtained in static DFT AbTTs, Ehlers *et al* [49] found that atomistic fracture behaviour was highly dependent on T and time, and argue for a new approach to obtaining traction separation laws that includes more sophisticated *ab initio* molecular dynamics than the rudimentary quasistatic approach used in our SGS test; healed metastable states like those presented during the separation of GBs in this paper can be extremely unstable at finite temperatures. However for small strains, big structural changes are unlikely to occur, even at $T \sim$ 300 K.

The reason the RGS + X and SGS tests have similar ΔH_{seg} values at δ_f for high Γ_H turns out to be a key result of this paper. Healing of a GB (figure 3) is characterised by substantial deformation of crystal structure. At the point of snapping the deformed structure collapses into two free surfaces with different morphology to pure RGS surfaces. For low Γ_H, ΔH_{seg} to SGS surfaces will be lower than to RGS surfaces because the healed GB collapses into a more stable structure which accommodates H. However higher Γ_H inhibits GB healing in SGS tests, resulting in similar free surface morphologies in SGS and RGS + X simulations. Figure 11 demonstrates this point where at low Γ_H (8 at%) there is significant healing such that at $\delta = 0.5$ nm there are still Al atoms across the interface that are in contact through a ligament structure. At higher coverages (40 at%) there is limited GB healing, yet some H can itself form connective interfacial ligaments. The lack of snapping observed in the homogenous straining calculation by Janisch *et al* [14] is only expected to be important in clean GBs, the reason for our snapping in $\Gamma_H = 0$ can be attributed to the different nature of the SGS test which does not unformally strain the CE cell and keeps a frozen core of bulk Al three atomic layers from the boundary. By maintaining a rigid bulk, deformation is limited to a decohering

plane. This approach does introduce some artificial rigidity to the system, but this was considered justifiable since it was discovered in [13] that homogenous straining simulations yield the same behaviour given large straining increments as RGS simulations which are inherently rigid. Furthermore, the point at which snapping occurs cannot accurately be obtained due to its necessary high sensitivity to separation increment size.

5. Conclusion

We have presented results of AbTTs of a $\Sigma 11$ Al GB using the established RGS/RGS + X approach and a revised SGS approach. We found that RGS + X and SGS tests show that H enrichment of the GB reduces the work of separation. Traction-separation laws were derived for these tests which demonstrate the gradual weakening of a GB as its H content increases and this result is a key requisite of HEDE. For important quantities, such as W and σ_c, RGS + X and SGS provide similar results. Therefore we conclude that the SGS method is a useful probe of fracture behaviour which in some cases will reduce the computation time of an AbTT; RGS + X will often involve more optimisation steps than a sequential SGS test which carries over information gathered in previous shifts to guide the geometry of the next. SGS tests have a further advantage of displaying atomistic fracture processes such as snapping and healing, although thermal activation may change this behaviour in a finite temperature regime.

We also discover small strains to a GB will substantially reduce the heat of segregation for H, which may have important consequences for models which include H diffusion rates that are relevant for crack propagation speeds. Diffusion rate modelling will need to be applied to elucidate the possibility of dynamic embrittlement under the level of reduction to the heat of segregation that we have shown. It is this information that is crucial to confirming the plausibility of HEDE operating in Al alloy systems, since the direct decohesion effect of lowering W and σ_c has now been firmly established for GBs with high levels of H enrichment.

Data availability statement

The data that support the findings of this study are available upon reasonable request from the authors.

Acknowledgments

BW is supported EPSRC Centre for Doctoral Training in Advanced Metallic Systems [EP/5022634/1], BW and PS are grateful for the support of Airbus. CPR was funded by a University Research Fellowship of the Royal Society. High performance computing was carried out using the University of Manchester's CSF3. Images showing atomic positions are produced using OVITO [50].

ORCID iDs

Benjamin T Wilson https://orcid.org/0000-0002-9007-7241
Joseph D Robson https://orcid.org/0000-0001-6115-4239
Pratheek Shanthraj https://orcid.org/0000-0002-6324-0306
Christopher P Race https://orcid.org/0000-0002-9775-687X

References

[1] Lynch S 2019 *Corrosion Rev.* **37** 377
[2] Hermann R 1988 *Corrosion* **44** 685
[3] Scully J R, Young G A and Smith S W 2012 *Gaseous H Embrittlement of Materials in Energy Technologies: The Problem, its Characterisation and Effects on Particular Alloy Classes* (Woodhead Publishing) pp 707–68
[4] Lynch S P 2011 *Stress Corrosion Cracking: Theory and Practice* (Cambridge: Woodhead Publishing) pp 90–130
[5] Liang S, Huang M, Zhao L, Zhu Y and Li Z 2021 *Int. J. Plast.* **143** 103023
[6] Lynch S 2012 *Corrosion Rev.* **30** 63
[7] Holroyd N J H and Scamans G M 2011 *Metall. Mater. Trans.* A **42** 3979
[8] Oriani R and Josephic P 1972 *Scr. Metall.* **6** 8
[9] Gerberich W 2012 *Gaseous H Embrittlement of Materials in Energy Technologies: Mechanisms, Modelling and Future Developments* (Cambridge: Woodhead Publishing) pp 209–46
[10] Tehranchi A and Curtin W A 2019 *Eng. Fract. Mech.* **216** 106502
[11] Rice J R and Wang J-S 1989 *Mater. Sci. Eng.* A **107** 23
[12] Ehlers F J H, Seydou M, Tingaud D, Maurel F, Charles Y and Queyreau S 2020 *Comput. Mater. Sci.* **173** 109403
[13] Van der Ven A and Ceder G 2004 *Acta Mater.* **52** 1223–35
[14] Janisch R, Ahmed N and Hartmaier A 2010 *Phys. Rev.* B **81** 184108
[15] Yamaguchi M, Ebihara K-I, Itakura M, Tsuru T, Matsuda K and Toda H 2019 *Comput. Mater. Sci.* **156** 368
[16] Rose J H, Smith J R and Ferrante J 1983 *Phys. Rev.* B **28** 1835
[17] Zhang S, Kontsevoi O Y, Freeman A J and Olson G B 2011 *Acta Mater.* **59** 6155
[18] Zhao D, Løvvik O M, Marthinsen K and Li Y 2018 *Acta Mater.* **145** 235
[19] Tahir A M, Janisch R and Hartmaier A 2013 *Modelling Simul. Mater. Sci. Eng.* **21** 075005
[20] Wang X and Benabou L 2018 *J. Eng. Mater. Technol.* **140** 011008
[21] Hajilou T, Taji I, Christien F, He S, Scheiber D, Ecker W, Pippan R, Razumovskiy V I and Barnoush A 2020 *Mater. Sci. Eng.* A **794** 139967
[22] Enrique R A and Van der Ven A 2017 *J. Mech. Phys. Solids* **107** 494
[23] Andric P and Curtin W A 2019 *Modelling Simul. Mater. Sci. Eng.* **27** 013001
[24] Wei X, Dong C, Chen Z, Xiao K and Li X 2016 *RSC Adv.* **6** 27282
[25] Martínez-Pañeda E, Golahmar A and Niordson C F 2018 *Comput. Methods Appl. Mech. Eng.* **342** 742
[26] Benabou L 2019 *Modelling Simul. Mater. Sci. Eng.* **27** 045007
[27] Zeiner P 2005 *Z. Kristallogr.* **220** 915–25
[28] Mishin Y, Sofronis P and Bassani J L 2002 *Acta Mater.* **50** 3609–22
[29] Paxton A T 2014 *Mater. Sci. Technol.* **30** 1063–70
[30] Sob M, Friak M, Legut D, Fiala J and Vitek V 2004 *Mater. Sci. Eng.* A **148** 378–89
[31] Kresse G and Hafner J 1993 *Phys. Rev.* B **47** 558
[32] Kresse G and Hafner J 1994 *Phys. Rev.* B **49** 14251
[33] Kresse G and Furthmüller J 1996 *Comput. Mater. Sci.* **6** 15
[34] Kresse G and Furthmüller J 1996 *Phys. Rev.* B **54** 11169
[35] Blöchl P E 1994 *Phys. Rev.* B **50** 17953
[36] Kresse G and Joubert D 1999 *Phys. Rev.* B **59** 1758
[37] Monkhorst H J and Pack J D 1976 *Phys. Rev.* B **13** 5188
[38] Perdew J P, Burke K and Ernzerhof M 1996 *Phys. Rev. Lett.* **77** 3865
[39] Perdew J P, Burke K and Ernzerhof M 1997 *Phys. Rev. Lett.* **78** 1396
[40] Methfessel M and Paxton A T 1989 *Phys. Rev.* B **40** 3616
[41] Davidson E R 1983 *Methods in Computational Molecular Physics* (*NATO Advanced Study Institute, Series C*) (Dordrecht, Holland: D. Reidel Publishing Company) p 95
[42] Teter M P, Payne M C and Allan D C 1989 *Phys. Rev.* B **40** 12255
[43] Bylander D M, Kleinman L and Lee S 1990 *Phys. Rev.* B **42** 1394
[44] Srirangarajan A, Datta A, Gandi A N, Ramamurty U and Waghmare U V 2014 *J. Phys.: Condens. Matter.* **26** 055006
[45] Park K and Paulino G H 2011 *Appl. Mech. Rev.* **64** 060802

[46] Lejček P, Šob M and Paidar V 2017 *Prog. Mater. Sci.* **87** 83–139
[47] Wright A F and Atlas S R 1994 *Phys. Rev.* B **50** 15248
[48] Martínez-Pañeda E, del Busto S, Niordson C F and Betegón C 2016 *Int. J. Hydrog. Energy* **41** 10265
[49] Ehlers F J H, Seydou M, Tingaud D, Maurel F, Charles Y and Queyreau S 2016 *Modelling Simul. Mater. Sci. Eng.* **24** 085014
[50] Stukowski A 2010 *Modelling Simul. Mater. Sci. Eng.* **18** 015012